The Cryosphere Discuss., 9, 609–653, 2015
www.the-cryosphere-discuss.net/9/609/2015/
doi:10.5194/tcd-9-609-2015

The Cryosphere
Discussions
Open Access

Modeling of crack propagation in weak snowpack layers using the discrete element method

J. Gaume[1], A. van Herwijnen[1], G. Chambon[2,3], J. Schweizer[1], and K. W. Birkeland[4]

[1]WSL Institute for Snow and Avalanche Research SLF, Davos, Switzerland
[2]Irstea, UR ETGR, Grenoble, France
[3]Université Grenoble Alpes, Grenoble, France
[4]USDA Forest Service National Avalanche Center, Bozeman, MT, USA

Received: 15 December 2014 – Accepted: 15 January 2015 – Published: 28 January 2015

Correspondence to: J. Gaume (gaume@slf.ch)

Published by Copernicus Publications on behalf of the European Geosciences Union.

Abstract

Dry-snow slab avalanches are generally caused by a sequence of fracture processes including (1) failure initiation in a weak snow layer underlying a cohesive slab, (2) crack propagation within the weak layer and (3) tensile fracture through the slab which leads to its detachment. During the past decades, theoretical and experimental work has gradually led to a better understanding of the fracture process in snow involving the collapse of the structure in the weak layer during fracture. This now allows us to better model failure initiation and the onset of crack propagation, i.e. to estimate the critical length required for crack propagation. On the other hand, our understanding of dynamic crack propagation and fracture arrest propensity is still very limited. For instance, it is not uncommon to perform field measurements with widespread crack propagation on one day, while a few days later, with very little changes to the snowpack, crack propagation does not occur anymore. Thus far, there is no clear theoretical framework to interpret such observations, and it is not clear how and which snowpack properties affect dynamic crack propagation. To shed more light on this issue, we performed numerical propagation saw test (PST) experiments applying the discrete element (DE) method and compared the numerical results with field measurements based on particle tracking. The goal is to investigate the influence of weak layer failure and the mechanical properties of the slab on crack propagation and fracture arrest propensity. Crack propagation speeds and distances before fracture arrest were derived from the DE simulations for different snowpack configurations and mechanical properties. Then, the relation between mechanical parameters of the snowpack was taken into account so as to compare numerical and experimental results, which were in good agreement, suggesting that the simulations can reproduce crack propagation in PSTs. Finally, an in-depth analysis of the mechanical processes at play was carried out which led to suggestions for minimum column length in field PSTs.

1 Introduction

Dry-snow slab avalanches result from the failure of a weak snow layer underlying cohesive slab layers. The local damage in the weak layer develops into a crack which can expand if its size exceeds a critical length or if the load exceeds a critical value. Finally, crack propagation leads to the tensile fracture of the slab and ultimately, avalanche release (McClung, 1979; Schweizer et al., 2003). During the past decade our understanding of the fracture process in snow has gradually evolved through the development of new theories as well as various field observations and experiments. The propagation saw test (PST), concurrently developed by Gauthier and Jamieson (2006) and Sigrist and Schweizer (2007), allows observers to determine the critical crack length and evaluate crack propagation propensity. This field method has highlighted the importance of slab bending (due to the collapsible nature of weak snow layers) on crack propagation (e.g. van Herwijnen et al., 2010; van Herwijnen and Birkeland, 2014). On the other hand, theoretical and numerical models, based on fracture mechanics or strength of material approaches, were developed to investigate crack propagation and avalanche release (McClung, 1979; Chiaia et al., 2008; Heierli et al., 2008; Gaume et al., 2013, 2014c). While substantial progress has been made, application with regard to avalanche forecasting or hazard mapping is still hindered in part by our lack of understanding of the dynamic phase of crack propagation. For instance, it is not uncommon to perform PST field measurements with widespread crack propagation on one day, while a few days later, with seemingly very little changes in snowpack properties, cracks will no longer propagate. Thus far, there is no clear theoretical framework to interpret such observations, and it is not clear how and which snowpack properties affect dynamic crack propagation. This limitation is due to the complex microstructure of snow and its highly porous character (Fig. 1) which are not taken into account in the continuous approaches previously mentioned.

In this paper, numerical experiments of the propagation saw test (PST) are performed applying the discrete element (DE) method which allows us to mimic the high porosity of snow. The goal is to investigate the influence of weak layer (WL) failure and the mechanical properties of the slab on crack propagation. In a first section, field data as well as the proposed model are presented. Then, crack propagation speed and distance before fracture arrest are derived from the DE simulations using the same method as for the field experiments (particle tracking). In a parametric analysis, we show the influence of single system parameters on the crack propagation speed and distance. Finally, the existing relation between snowpack properties is accounted for in order to compare numerical and experimental results and the mechanical processes leading to fracture arrest are analysed.

2 Data and methods

2.1 PST field data

Since the winter of 2002–2003, we collected data from 121 PST experiments at 46 different sites in Canada, USA and Switzerland (van Herwijnen and Jamieson, 2005; van Herwijnen and Heierli, 2009; van Herwijnen et al., 2010; Bair et al., 2012; van Herwijnen and Birkeland, 2014; Birkeland et al., 2014). At each site, we collected a manual snow profile and conducted one or several PSTs according to the procedure outlined in Greene et al. (2004). In many cases we used longer (than standard) beams to allow us to better investigate crack propagation. After PST preparation, we inserted black plastic markers into the pit wall and used a digital camera on a tripod to make a video recording of the PST (Fig. 2). We used a particle tracking velocimetry (PTV) algorithm to analyze the motion of the markers and thus the displacement of the snow slab above the weak layer (Crocker and Grier, 1996). In this way, the position of the markers in each video frame can be determined with a mean accuracy of 0.1 mm. The displacement of a marker is then defined as the movement relative to its initial position, that is, the average position of the marker prior to movement. For propagating cracks, there is a delay between the vertical displacement of subsequent markers. A typical displacement time-evolution for a propagating crack is shown in Fig. 3 for four slab markers. As explained in van Herwijnen and Jamieson (2005), the time delay between the onset of movement between markers is proportional to the distance between the markers and was used to calculate the propagation speed c of the fracture.

2.2 Discrete element model

2.2.1 Motivation and objectives

Discrete element (DE) modeling (Cundall and Strack, 1979) allows computing the motion of a large number of small grains by solving dynamic equations for each of them and defining a contact law between the grains. In addition, the DE method allows assessing mechanical quantities such as stress, displacement, deformation rate, porosity, etc. computed over representative elementary domains at each material point within the sample. Experimentally, this would be an impossible task. Hence, using DE, the mechanical and rheological behavior of the material can be explored locally, regardless of the spatial heterogeneities possibly displayed by the structure of the material and its mechanical quantities. This method can thus help to better understand physical processes at play in granular assemblies. The DE method has been widely used to study the flow of granular materials within industrial (e.g. Chaudhuri et al., 2006; Sarkar and Wassgren, 2010) or environmental applications such as snow dynamics (e.g. Rognon et al., 2008; Faug et al., 2009). However, to our knowledge, discrete elements have never been used to model crack propagation in layered systems or to describe slab avalanche release processes. The latter processes are generally modeled under a continuum mechanics framework, using methods such as finite elements (Podolskiy et al., 2013, and references therein). While these methods can be used to assess the stability of a layered snow cover, i.e. determine the conditions of failure occurrence and the onset of crack propagation, they are not suited to study what occurs after failure, i.e. during the dynamic phase of crack propagation, due to a lack in relevant constitutive models for the WL. The objective of the proposed approach is to use the DE method to model the structure of both the slab and the WL using discrete cohesive grains. This will allow mimicking the high porosity of the WL and to account for slab elasticity and for the different modes of failure possibly displayed by snow (shear, compression, tension). Ultimately, DE propagation saw tests will be performed to investigate the characteristics of crack propagation.

2.2.2 Formulation of the model

The discrete element simulations were performed using the commercial software PFC2D (by Itasca), which implements the original soft-contact algorithm described in Cundall and Strack (1979). The simulated system is two dimensional and is composed of a completely rigid basal layer, a WL of thickness D_{wl} and a slab of thickness D which were varied in the simulations. The slab is composed of grains of radius $r = 0.01\,\mathrm{m}$ with a primitive cubic packing. The porosity of the slab is equal to 21 %. Hence the density of the slab ρ can be adjusted by changing the grain density $\rho_{\mathrm{p,s}}$ (varied in the simulations). The WL is composed of grains of radius $r_{\mathrm{wl}} = r/2$ with a complex packing of collapsible triangular forms aimed at roughly representing the porous structure of persistent WLs such as surface hoar or depth hoar. The porosity of the WL is 70 % and the density of the WL grains is $\rho_{\mathrm{p,wl}} = 400\,\mathrm{kg\,m^{-3}}$, leading to a WL density $\rho_{\mathrm{wl}} = 120\,\mathrm{kg\,m^{-3}}$. The length of the system (column length) is $L = 2\,\mathrm{m}$ and the slope angle is denoted ψ. It is worth noting that the numerical grains are not indented to represent the real snow grains which are obviously smaller and have a different density. Nevertheless, as will be shown, this set up allows to capture the main features observed in field PSTs.

The loading is applied by gravity and by advancing a "saw" (in red on Fig. 4a) at a constant velocity $v_{\mathrm{saw}} = 2\,\mathrm{m\,s^{-1}}$ through the weak layer. This saw is composed by rigid walls and has approximately the same thickness as field saws $h_{\mathrm{saw}} = 2\,\mathrm{mm}$. The saw velocity was chosen relatively high to decrease the computational time, but lower than the lowest crack propagation speed observed in the field so as to correctly distinguish crack propagation from the saw movement.

A classical contact law was used in the simulations (Radjai and Dubois, 2011; Gaume et al., 2011). The normal force is the sum of a linear elastic and of a viscous contribution (spring-dashpot model), and the tangential force is linear elastic with a Coulombian friction threshold. The corresponding mechanical parameters, namely the normal and shear stiffness k_n and k_s (elasticity parameters), the restitution coefficient e (viscous parameter) and the friction coefficient μ are summarized in Table 1. The value of the normal stiffness k_n was chosen in such a way that the normal interpenetrations at contacts are kept small, i.e. to work in the quasi-rigid grain limit (da Cruz et al., 2005; Roux and Combe, 2002). Concerning the normal restitution coefficient e, we verified that the results presented below, and more generally all the macroscopic mechanical quantities obtained from the simulations, are actually independent of this parameter (in the range 0.1–0.9).

Cohesion was introduced by adding a bond at each contact (Fig. 4b). A contact bond can be envisioned as a point of glue with constant normal and shear stiffness k_n^b and k_s^b acting at the contact point (Fig. 4b). This bond has a specified shear and tensile strength σ_s and σ_t. The maximum tensile and shear stresses σ_max and τ_max at the bond periphery are calculated via beam theory according to:

$$\sigma_\mathrm{max} = -\frac{F_\mathrm{n}}{A} + \frac{|M| r_\mathrm{b}}{I} \tag{1}$$

$$\tau_\mathrm{max} = \frac{|F_\mathrm{s}|}{A} \tag{2}$$

where F_n and F_s are the bond normal and shear forces, $|M|$ is the bending moment, r_b the bond radius, $A = \pi r_\mathrm{b}^2$ the bond area and $I = \pi r_\mathrm{b}^4/4$ its moment of inertia. If the magnitude of the tensile stress exceeds the bond tensile strength, the bond breaks and both the normal and shear contact forces are set to zero. If the magnitude of the shear stress exceeds the bond shear strength, the bond also breaks but the contact forces are not altered, provided that the shear force does not exceed the friction limit, and provided that the normal force is compressive. The ranges of parameters used for the bond model are summarized in Table 2.

2.2.3 Simulation protocol and illustration

First, the macroscopic properties of the slab have to be determined as a function of the microscopic properties of the bond. Hence, bi-axial tests were carried out and allowed to determine the macroscopic Young's modulus of the slab as a function of the bond stiffness. Similarly, simple loading tests were carried out to compute the macroscopic failure criterion (mixed mode shear-compression) of the WL as a function of the bonds of WL grains (Gaume et al., 2014b).

Then, PST simulations were performed. An illustration of a simulation result highlighting the displacement wave of the slab is shown in Fig. 5 and the associated vertical displacement Δy is represented in Fig. 6. The critical length is denoted a_c and corresponds to the translation length of the saw required to obtain self crack propagation.

In order to determine the crack propagation speed, purely elastic simulations (infinite tensile and shear strength of the bonds between particles in the slab) were carried out. The propagation speed was computed using the same method as for field PSTs by analyzing the vertical displacement wave of the slab (van Herwijnen and Jamieson, 2005). The only difference with the procedure for field measurements is that with DE we do not need markers since we have access to the displacement of every grain of the system.

The propagation distance was computed by taking into account the possible failure of the slab by setting finite values to the tensile and shear strength of the slab (σ_t, σ_s). We define the propagation distance as the distance between the left wall of the system and the crack tip of the slab, as shown in Fig. 7. This measure of the propagation distance differs from the one defined originally by Gauthier and Jamieson (2006) who defined it as the distance between the point of onset of crack propagation in the WL and the point of slab failure. However, we argue that the propagation distance, as we defined it, is a more suitable measure since this is the one that influences the stresses in the slab and thus fracture arrest propensity.

For the parametric analysis (Sect. 3.2), we performed simulations for which only one system parameter was modified while the other parameters were kept constant. The parameters used are described in Table 3. However to apply these results to slab avalanche release and in order to compare our results to field data (Sect. 3.2), existing relations between snowpack properties were taken into account. Hence, simulations were performed for different slab densities with a Young's modulus varying according to an empirical exponential fit to the data reported by Scapozza (2004):

$$E = 1.873 \times 10^5 e^{0.0149\rho}, \tag{3}$$

and with a tensile strength varying according to a power-law fit of the data reported by Sigrist (2006):

$$\sigma_\mathrm{t} = 2.4 \times 10^5 \left(\frac{\rho}{\rho_\mathrm{ice}}\right)^{2.44} \tag{4}$$

with $\rho_\mathrm{ice} = 917\,\mathrm{kg\,m^{-3}}$.

3 Results

3.1 Displacement of the slab

The evolution of the vertical displacement of the slab Δy is represented in Fig. 6. On this figure together with the illustration of the displacement wave of the slab (Fig. 5), one can clearly observe the different processes acting before, during and after crack propagation. First, slab bending occurs prior to the onset of crack propagation and the dynamic propagation phase. These distinct phases (stable bending of the slab and crack propagation) are also clearly visible in the vertical displacement Δy, as shown in Fig. 6 for four different horizontal positions in the slab.

Between 0 and 0.1 s nothing happens, then as the saw advances, the vertical displacement slowly increases. This phase corresponds to the bending of the slab on the left side of the saw. Then, for $t = 0.25$ s approximately, the critical length a_c was reached and the displacement increases abruptly, even beyond the saw, corresponding to the dynamic crack propagation phase. After $t = 0.3$ s, the slab has reached the broken WL at the left-end of the slab for $x = 0$ m. After 0.32 s, the entire WL has collapsed leading to a constant vertical displacement of the slab approximately equal to $\Delta y = 1.8$ cm. This displacement is not perfectly equal to the WL thickness because of the grains remaining in the WL. The peak in the displacement around $t = 0.38$ s is an artefact associated to the movement of the saw after the crack has propagated which does not affect the results that we will present.

3.2 Parametric analysis

3.2.1 Crack propagation speed

For all the simulations carried out, the crack propagation speed varied between 5 and 60 $\mathrm{m\,s^{-1}}$. Figure 8a shows that the crack propagation speed c strongly increases with the Young's modulus of the slab E, from almost zero for a very soft slab ($E \approx 0.5$ MPa) to 40 $\mathrm{m\,s^{-1}}$ for a rigid slab ($E \approx 50$ MPa) where the increase levels off. The propagation speed c also strongly and linearly increases with the thickness of the slab D (Fig. 8b), from almost zero for a slab thickness lower than 10 cm to 60 $\mathrm{m\,s^{-1}}$ for a thickness of 80 cm. Similar to the increase with slab thickness, the propagation speed increases almost linearly with the density of the slab ρ (Fig. 8c) and the slope angle ψ (Fig. 8d). The propagation speed seems not to be influenced by the thickness of the WL (Fig. 8b) as soon as the failure occurs under the same conditions (same critical length). This suggests that the crack propagation speed is mostly influenced by the failure conditions (load due to the slab and WL strength) rather than structural parameters such as the WL thickness.

3.2.2 Propagation distance

Figure 9 shows propagation distance as a function of different system parameters. Figure 9a$_1$, b$_1$ and c$_1$ shows the increase of the propagation distance with increasing tensile strength of the slab σ_t. This result was expected since a stronger slab requires a larger tensile stress in order to break and thus a larger propagation distance is required to obtain sufficient tensile stresses in the slab (induced by bending or by the shear component of the the slab's weight additionally in case of $\psi \neq 0$).

The influence of the Young's modulus E of the slab is shown in Fig. 9a$_1$ and a$_2$. Overall, propagation distance decreases in general with increasing Young's modulus. Hence, the softer the slab is, the lower is the fracture arrest propensity. For a tensile strength of 2 kPa (Fig. 9a$_2$), the propagation distance l^* sharply decreases from 2 m (column length) to an approximately constant value $l^* = 0.5$ m for $E \approx 2$ MPa. Also, Fig. 9a$_1$ shows that for higher Young's modulus larger tensile strength values are required to obtain full propagation. The critical length a_c for crack propagation was also represented in Fig. 9a$_2$ to show that the tensile failure across the slab always occurred (in this case) after the onset of crack propagation.

Then, the influence of WL thickness D_{wl} is shown in Fig. 9b$_1$ and b$_2$. The WLs have different thicknesses but the same failure criterion and thus the same critical length a_c which is equal to 15 cm in this case. The propagation distance l^* decreases with increasing WL thickness. For low values of the tensile strength of the slab, the propagation distance is small and almost independent of the WL thickness whereas an important decrease is observed for larger values of the tensile strength. In other words, this finding means that thicker weak layers result in more slab bending so that slab failure becomes more likely due to high tensile (bending) stress.

Figure 9c$_1$ and c$_2$ shows the influence of slope angle ψ on propagation distance. Similarly to WL thickness, slope angle seems to have no influence on the propagation distance for low values of the tensile strength. However, for larger values of σ_t ($\sigma_t >$ 3.5 kPa), the propagation distance strongly increases with increasing slope angle ψ.

Hence, fracture arrest propensity decreases with slope angle. This result is not trivial, since as the slope angle increases, there is a competition between the decreasing slab bending which results in a decrease of the tensile stresses in the slab and an increase of the tensile stresses due to the weight of the slab in the slope parallel direction. Hence, this result suggests that slab bending is the primary process influencing tensile failure of the slab (for homogeneous properties of the system). This interpretation is supported by the observation that the tensile opening of the crack always starts from the top surface of the slab in both DE simulations (Fig. 7) and in field PSTs.

Crack propagation distance slightly decreases with slab density as shown in Fig. 9d. For very low slab densities, the critical length a_c is relatively high and thus the tensile failure across the slab occurs before the critical length is reached. Then, as the density of the slab increases, the critical length decreases and the propagation distance stabilizes around 0.4 m.

Finally, whereas slab density ρ and slab thickness D have a similar influence on the stability of the system and on the onset of crack propagation, as suggested by the decrease of the critical length a_c with both ρ and D, this is certainly not true for their influence on fracture arrest propensity. Indeed, in contrast to the influence of slab density, the propagation distance strongly increases with increasing slab thickness (Fig. 9e). Hence, the thicker the slab is, the lower is the fracture arrest propensity. This results can be easily explained using beam theory (Timoshenko and Goodier, 1970) to express the tensile stress in a bending slab which is inversely proportional to the slab thickness D (see Sect. 3.4 or Schweizer et al., 2014).

3.3 Comparison with field data

The findings of the preceding parametric analysis have to be interpreted with care since for snow, several of the system parameters are inter-related leading to more complicated outcomes. As an example, the decrease of the propagation distance with Young's modulus seems to be in contradiction with field experiments. Indeed, this result suggests that stiff and thus hard snow slabs would be associated to smaller release zones than soft slabs which is obviously in contradiction with avalanche observations (van Herwijnen and Jamieson, 2007). Therefore, even if the result evidenced by Fig. 9a$_2$ is mechanically consistent, no firm conclusions can be directly drawn with regards to dry-snow slab avalanche release. To this end, the relationships between slab density ρ, Young's modulus E and tensile strength σ_t need to be considered according to Eqs. (3) and (4). Simulations were performed for slab densities ranging from 100 to 300 $\mathrm{kg\,m^{-3}}$, corresponding to a Young's modulus E of the slab between 0.8 and 16 MPa (Eq. 3) and a tensile strength σ_t between 1 and 16 kPa (Eq. 4).

In the following, we distinguish two simulation cases:

- *Case #1* corresponds to simulations with a constant slab thickness $D = 20$ cm, slope angle $\psi = 0^\circ$ and WL properties;
- *Case #2* corresponds to a case with a slope angle $\psi = 23^\circ$ which is the average slope angle of our field PSTs and a slab thickness D which is also a function of density according to field data (Table 4). In addition, we calibrated the strength of the WL bonds in order to have the same critical length for the different densities. This ensured we observed crack propagation and avoid the global and simultaneous failure of the entire WL. Indeed, as density increases, the critical length a_c decreases and tends to zero (Fig. 9d) leading to the instability of the system without cutting the WL.

3.3.1 Displacement of the slab

Our numerical results (Fig. 6) obtained for a slab density $\rho = 250\,\mathrm{kg\,m^{-3}}$ are in very good agreement with experimental results (Fig. 3) obtained for a similar density of $\rho = 240\,\mathrm{kg\,m^{-3}}$. Indeed, the same phases in the displacement curves, corresponding to slab bending and crack propagation, were observed in the measurements. Furthermore, the amount of slope normal displacement prior to crack propagation as well as the fracture time, defined as the time it takes for the slab to come into contact with the broken weak layer, were very similar. Finally, we would like to point out that the total slope normal displacement after crack propagation in our experimental results was not the same for all markers (Fig. 3), which has often been observed in previous studies (van Herwijnen et al., 2010; Bair et al., 2014), whereas it is approximately the same in the numerical simulations if no fracture arrest occurred (Fig. 6). This is presumably due to 3-D and edge effects such as wall friction at the right interface.

3.3.2 Crack propagation speed

The crack propagation speed c obtained in field PSTs and from the simulated PSTs is represented as a function of slab density in Fig. 10. Overall, the propagation speed obtained from field PSTs increases from 10 to 50 $\mathrm{m\,s^{-1}}$ as the density of the slab increased from 140 to 300 $\mathrm{kg\,m^{-3}}$. The gray squares represent the cases with fracture arrest due to tensile fracture of the slab (SF: "Slab Fracture") for which the crack propagation speed is not very accurate and generally lower than the velocity measured when the slab did not break (END: empty squares for full propagation until the "end" of the system).

Overall, both simulation cases #1 and #2 reproduce the magnitude of the propagation speed c and the increasing trend with increasing slab density ρ. The case #2 model (relation between slab density, Young's modulus, thickness and slope angle) slightly overestimates the average propagation speed for low slab densities but provides good estimates for densities higher than 250 $\mathrm{kg\,m^{-3}}$. The slight overestimation for low densities might be due to the fact that, to compute the propagation speed, the slab was considered as purely elastic and possible plastic effects in the slab that might induce energy dissipation were disregarded. Furthermore, the simulations of case #2 have been done for the same conditions of failure initiation, i.e. the strength of the WL bonds have been calibrated in order to have the same critical length for the different densities. This is not the case for the experiments for which the critical length generally increases with increasing density due to the associated increase of Young's modulus and a strengthening of the WL (Zeidler and Jamieson, 2006a, b; Szabo and Schneebeli, 2007; Podolskiy et al., 2014). In contrast, for case #1, a decrease in slab thickness and slope angle induces a decrease in the crack propagation speed (Fig. 8), explaining why the model result for case #1 ($\psi = 0^{\circ}$ and $D = 20$ cm) gives lower speed values. Furthermore, for case #1, the WL properties were kept constant, which together with the increase of Young's modulus (less bending) with density resulted in an increase of the critical length with density, in agreement with field observations which might explain the better quantitative agreement with the experiments.

3.3.3 Propagation distance

The proportion between the number of experiments for which fracture arrest was observed N_{SF} and the total number of experiments $N_{SF} + N_{END}$ is shown vs. slab density ρ in Fig. 11a. This figure highlights the important decrease of fracture arrest propensity with slab density. Slab densities higher than 300 kg m^{-3} lead to a very small amount of experiments with slab fracture ($N_{SF} < 20$ %).

The crack propagation distance l^* is represented as a function of slab density in Fig. 11b. Only cases with slab fracture (SF) were represented. Overall, the propagation distance obtained from field PSTs increased with slab density and varies approximately from 0.4 to 2.1 m as the density increased from 140 to 300 kg m^{-3}. This trend is well reproduced by the discrete element simulations for both cases, but with a better qualitative agreement for case #1. For case #1 and for densities higher that about 300 kg m^{-3}, no fracture arrest is observed resulting in full propagation of the crack in the WL (END) over the entire column length. For case #2, this transition occurs already for a density of about 200 kg m^{-3}. Besides, we would like to point out that cases of field PSTs with fracture arrest were made for different column lengths. However, we argue that, as soon as fracture arrest occurs within the beam, the crack propagation distance is almost independent of the beam length. For instance, if a propagation distance of 0.7 m is observed for a column length of 1.5 m, it would certainly be the same for a column of 2.5 m, as soon as the column length is higher than the length over which edge effect are observed (length typically lower than 1 m, Gaume et al., 2013).

The experiments and the simulations confirm that dense and hard snow slabs are more prone to wide-spread crack propagation than soft slabs.

3.4 Mechanical processes of fracture arrest

In order to better understand the underlying mechanical processes of fracture arrest in the slab, the tensile stresses in the slab σ_{xx} have to be compared with its tensile strength σ_t. A tensile crack in the slab occurs when the maximum tensile stress σ_{xx}^m meets the tensile strength. Hence, we analyzed the evolution of the tensile stresses in the slab during the process of crack propagation for case #1 with a slab density $\rho = 250\,\mathrm{kg\,m^{-3}}$ leading to a tensile strength $\sigma_\mathrm{t} = 10\,\mathrm{kPa}$ (Eq. 4). Figure 12 shows the tensile stresses in the slab for different stages of the propagation process. First, before the onset of crack propagation, an increase of tensile stress occurs at the top of the slab close to the crack tip of the WL. The bottom of the slab is subjected to an increase in compression ($\sigma_{xx} < 0$). This increase of tensile stress is due to the bending of the slab and increases with increasing crack length (Timoshenko and Goodier, 1970).

Then, once the critical length is reached, the crack becomes self-propagating. The crack length increase leads to an increase of the tensile stresses in the slab. Note that the maximum tensile stress σ_{xx}^m is always located at the top surface of the slab, not directly at the vertical of the crack tip but slightly shifted towards the right side. At one point the maximum tensile stress meets the tensile strength of the slab ($\sigma_\mathrm{t} = 10\,\mathrm{kPa}$) which leads to the tensile crack opening and fracture arrest. This fracture arrest leads to the unloading of the slab where the stresses are close to zero everywhere, except at the position of the saw where some small local bending effects still occur.

In order to better understand why fracture arrest does not occur anymore for large densities, as shown in Fig. 11, we then analyzed the maximum tensile stress σ_{xx}^m as a function of slab density in the case of a purely elastic slab for which the Young's modulus was varied according to Eq. (3) (case #1). The DE results were then compared to those predicted by the static beam theory. According to beam theory (Timoshenko and Goodier, 1970), the maximum theoretical tensile stress in a beam of length l, thickness D embedded on its right side and subjected to gravity, with an angle ψ (with regards to the horizontal) is equal to

$$\sigma_{xx}^{\mathrm{th}} = \rho g l \sin\psi + \frac{3\rho g \cos\psi l^2}{D}. \tag{5}$$

As we have seen before on Fig. 12, the tensile stress in the slab increases during propagation due to an increase of the crack length. However, this length is limited by the amplitude of collapse of the WL h_c (Fig. 13a). Indeed, once the left part of the slab comes into contact with the broken WL, then the tensile stress does not increase any further, but has reached its maximum value (see also Fig. 5c). The length l_0 (already introduced by Heierli et al., 2008) required to come into contact with the broken WL can be obtained analytically by computing the vertical displacement of the slab according to beam theory and is equal to

$$l_0 = \left(\frac{2ED^2h_c}{3\rho g\cos\psi}\right)^{1/4}. \tag{6}$$

Hence, the overall maximum theoretical tensile stress $\sigma_{xx}^{\mathrm{m,th}} = \sigma_{xx}^{\mathrm{th}}(l_0)$ is found by replacing l by l_0 in Eq. (5).

For low values of slab's density ($\rho < 175\,\mathrm{kg\,m^{-3}}$, Fig. 13b), the maximum tensile stress increases with increasing density and the DE model results are very well reproduced by beam theory. In addition, the maximum tensile stress is always higher than the tensile strength of the slab, leading to systematic fracture arrest for these low density values. However, for higher densities, beam theory predicts a strong increase of the maximum tensile stress with density, so that the stress would always be higher than the tensile strength of the slab. This would lead to systematic fracture arrest for any value of the density which is in contrast to the results of both field and numerical PSTs. The DE model results, in particular, show that for a slab density higher than about 180 kg m^{-3}, the maximum tensile stress starts to decrease with increasing density. Ultimately, for a density of approximately 280 kg m^{-3}, the maximum tensile stress becomes lower than the strength leading to full propagation of the crack in the WL, in agreement with Fig. 11 (case #1).

This result highlights the limits of the static beam theory and thus the need to take into account dynamic effects when addressing fracture arrest propensity issues. Indeed, we suppose that the reason of this sudden decrease is due to the crack propagation speed which becomes higher as slab density increases and induces a loss of support in the slab where stresses do not have time to establish. For instance, if we assume that the crack would propagate at an infinite speed, then the tensile stresses in the slab would not increase after reaching the critical length. The maximum tensile stress in the slab would thus be the one obtained at the moment of the onset of crack propagation. Obviously, the propagation speed is not infinite but limits the establishment of the stresses in the slab. Based on the observed decrease beyond 180 kg m^{-3} (Fig. 13b), we propose an empirical relation describing the maximum tensile stress:

$$\sigma_{xx}^{\mathrm{m,th}} = \alpha_{\mathrm{dyn}}(\rho)\sigma_{xx}^{\mathrm{th}}(l_0) = e^{-\frac{\rho-\rho'}{r}}\sigma_{xx}^{\mathrm{th}}(l_0), \quad \text{for } \rho > \rho' \tag{7}$$

with $\rho' = 179$ kg m^{-3} and $r = 35$ kg m^{-3}. The value of ρ' hence represents the transition point beyond which beam theory does not apply anymore (dashed/dotted line in Fig. 13b). Note that more generally, α_{dyn} is likely to depend not only on slab density ρ, but also on the crack propagation speed c and on the slab Young's modulus E, which are anyhow related to slab density explaining why in this case ρ is the main driving parameter.

Using the theoretical relationships for both zones ($\rho < \rho'$ and $\rho > \rho'$) one can compute the theoretical propagation distance l_{th}^* by solving

$$\sigma_{xx}^{\mathrm{m,th}}(l_{\mathrm{th}}^*) = \sigma_{\mathrm{t}}. \tag{8}$$

The theoretical propagation distance l_{th}^* was represented in Fig. 13c for both zones (l_{bt}^* for $\rho < \rho'$ and $l_{\mathrm{dyn}}^*\rho > \rho'$) as well as the characteristic distance l_0. Again, the beam theory reproduces well the results for low densities. For these low densities, the tensile failure in the slab occurs even before the onset of crack propagation due to the low value of the associated tensile strength. However, the important increase of the propagation distance for densities higher than ρ' is not reproduced by beam theory. On the other hand, using the empirical relation (Eq. 7), the strong increase of the propagation distance is well reproduced. After a certain value of density $\rho^{\mathrm{END}} = 280\,\mathrm{kg\,m^{-3}}$, the propagation distance l^*_{dyn} becomes higher than l_0 which is technically not possible since the maximum tensile stress is obtained exactly for $l = l_0$ and cannot increase above l_0. Hence the only solution is that no fracture arrest occurs for $\rho > \rho^{\mathrm{END}}$. In fact, for a density of $300\,\mathrm{kg\,m^{-3}}$ no fracture arrest was observed using the DE model (Fig. 11). For this simulation, we also tried with longer column lengths L up to 10 m which did not affect the full propagation. The corresponding maximum propagation distance for this case is about 2.3 m (for $l^*_{\mathrm{dyn}} = l_0$), in agreement with field data for which the maximum propagation distance recorded for was $l^* = 2.15\,\mathrm{m}$ (Fig. 11b).

Obviously, the density ρ^{END} which was $280\,\mathrm{kg\,m^{-3}}$ in our simulations, will vary depending on the geometry and material properties of the snowpack. For the cases presented in Fig. 13b and c, the Young's modulus was derived from density (Eq. 3), the slab thickness D was constant equal to 20 cm, the slope angle $\psi = 0^\circ$ (case #1). This set of parameters resulted in a density $\rho^{\mathrm{END}} = 280\,\mathrm{kg\,m^{-3}}$. However, for a slope angle of 23° and taking into account the dependence of slab thickness with slab density (Table 4), ρ^{END} would be even smaller than $200\,\mathrm{kg\,m^{-3}}$ as shown in Fig. 11b (case #2) since the transition between a regime of fracture arrest and full propagation is between 150 and $200\,\mathrm{kg\,m^{-3}}$. Furthermore, the propagation distance being also strongly influenced by the WL thickness D_{wl} (Fig. 9b), we assume that ρ^{END} increases with D_{wl} as the maximum tensile stress in the slab increases with D_{wl}.

4 Discussion

In this study, a numerical model based on the discrete element method was developed in order to perform numerical PST simulations and study the mechanical processes involved. Despite the apparent simplicity of the proposed DE model and of the structure of the simulated WL, we were able to quantitatively address the issue of the dynamic phase of crack propagation as well as fracture arrest propensity and to reproduce PST field data.

First, a parametric analysis was conducted to study the influence of snowpack properties on crack propagation speed on the propagation distance. It was shown that the propagation speed increases with increasing slab density ρ, slab Young's modulus E, slab thickness D and slope angle ψ. The propagation speed was almost not influenced by the WL thickness. The increase of crack propagation speed with slab density is not compatible with the expression for crack propagation speed proposed by Heierli (2008) for which the speed decreases with increasing slab density ρ, as for a crack in a homogeneous material (Auld, 1973). However, this is obviously not the case here, since the crack propagates through the underlying WL. Therefore, the propagation speed is likely to decrease with increasing WL density (and thus to increase with increasing WL porosity) but to increase with slab density, as shown by our results.

In addition, it was shown that the propagation distance l^* increases with increasing tensile strength of the slab σ_t, slab thickness D and slope angle ψ. The latter result together with the fact that the tensile opening of the crack in the slab always occurs from the top surface, suggests that slab bending is the primary process influencing the tensile failure of the slab. On the contrary the propagation distance decreases with increasing slab Young's modulus E, slab density ρ and WL thickness D_{wl}. These results are in agreement with Gaume et al. (2014a) who showed that the tensile failure probability (fracture arrest propensity) decreased with increasing tensile strength σ_t of the slab, increased with increasing Young's modulus E of the slab and decrease with increasing slab thickness D.

Furthermore, by accounting for the relation between the mechanical properties of the snowpack, the increase of crack propagation speed and distance with increasing slab density could be well reproduced. The in-depth analysis of the mechanical processes involved in fracture arrest showed that after a certain value of the slab density ρ', the evolution of the maximum tensile stress in the slab with slab density diverged from the static beam theory. This is due to dynamic effects during crack propagation that induce a loss of support of the slab where the stresses do not have time to establish. Ultimately, for a density ρ^{END}, the maximum tensile stress in the slab decreases below its tensile strength leading to full propagation without fracture arrest. Consequently, for large densities, mechanical properties of the snowpack only marginally affect crack propagation distance. In that case, terrain characteristics and snowpack spatial variability will play a crucial role in the definition of the release area.

In addition, interestingly, in very few simulations both fracture arrest by tensile failure of the slab and full propagation was observed. In these cases, a portion of the WL on the right-side of the slab tensile crack was damaged over a sufficient length to exceed the critical length leading again to crack propagation. This process repeated itself until the end of the system leading to the so-called “en-echelon” fracture (Gauthier and Jamieson, 2010). This is likely to happen for very unstable conditions (very low critical length) but for a slab of intermediate density, not too dense so fracture arrest can occur and not too loose so that the crack can propagate.

Concerning the limitations of the model, we recall that the triangular shape of the WL structure is highly idealized and that more complex and more realistic geometries might have an influence on the presented results. In the future, the micro-structure of the WL could be derived from micro-tomographic images (Hagenmuller et al., 2014) in order to perform more realistic simulations. Moreover, we would like to recall that the crack propagation speed was computed from the vertical displacement wave of the slab. However, for high values of the slope angle ψ, the collapse only constitutes a secondary process and the tangential displacement during propagation becomes higher than the vertical displacement. Typically, for $\psi > 40^{\circ}$, it is not possible to compute the propagation speed using the presented approach as the height of collapse becomes too low. A preliminary and still incomplete analysis of the tangential displacement revealed that the crack propagation speed of slopes for which the shear component of the slab weight is very important ($\psi > 40^\circ$) might be significantly higher than the propagation speed on flatter slopes. This analysis suggested propagation speeds up to $150\,\mathrm{m\,s^{-1}}$, similar to those observed in the field for real-scale avalanches by Hamre et al. (2014). However, they considered avalanches triggered artificially by explosives leading to even more complex interactions due to the propagation wave of the blast.

In regards to practical applications, the results of our study can help to choose the size of the column length in field PSTs. Indeed, we showed that the maximum length for which snowpack properties might affect the propagation distance is around 2 m, in agreement with the study of Bair et al. (2014). However, this result does not mean that all PSTs should be 2 m long. The chosen column length can be evaluated from slab thickness and density. As shown by Figs. 9 and 11, slab Young's modulus and tensile strength which are related to slab density, as well as slab thickness strongly affect the propagation distance. Hence, for soft and relatively thin slab, the standard column length of 1.2 m might be sufficient. However, for very strong and thick slabs, the column length of the PST should not be lower than 2 m in order to be able to still observe a possible arrest of the fracture due to slab tensile failure. If slab fracture is not observed in a PST for a column length of 2 m, fracture arrest is likely to be mainly driven by terrain and snowpack spatial variability and a 3-D-terrain model with snowpack might be required to evaluate where fracture arrest might occur (Veitinger et al., 2014).

5 Conclusions

We proposed a new approach to characterize the dynamic phase of crack propagation in weak snowpack layers as well as fracture arrest propensity by means of numerical PST simulations based on the discrete element method with elastic-brittle bonded grains.

This model allowed us to compute crack propagation speed from slab vertical displacement as a function of snowpack properties. Furthermore, crack propagation distance was computed by taking into account the tensile strength of the slab. A parametric analysis allowed us to compute the crack propagation speed and distance as a function of the different snowpack properties. Then, the existing relationship between slab thickness, Young's modulus and tensile strength with density was implemented. Accounting for this relationship, modeled propagation speed and distances were found in good agreement with those obtained from field measurements of propagation saw test. In particular, for densities ranging from 100 to 300 $\mathrm{kg\,m^{-3}}$, the propagation speed increased from approx. 10 to 50 $\mathrm{m\,s^{-1}}$ and the propagation distance was found to increase from approx. 0.4 to 2 m (column length). Concerning the mechanical processes, the static beam theory predicts an increase of the maximum tensile stress with increasing density. However, we show that dynamic effects of crack propagation induce a loss of support of the slab which increases with increasing crack propagation speed and thus slab density. This produces a decrease of maximum stress with density which ultimately becomes lower than the tensile strength of the slab for a critical density ρ^{END} leading to the absence of slab tensile fracture and thus wide-spread crack propagation. According to our simulations, this critical density depends mostly on slab and WL thicknesses and slope angle. It decreases with slab depth and slope angle but increases with WL thickness.

For slab layers denser than ρ^{END}, the slab tensile fracture in the field and thus the potential release size will be mostly controlled by topographical and morphological features of the path such as ridges, rocks, trees, terrain breaks, etc. but also by the spatial heterogeneity of the snow cover. In addition, we showed that the maximum propagation distance associated with the density ρ^{END} was around 2 m, justifying why the beam length of a propagation saw test should not be lower than 2 m for hard snow slabs, in order to be able to observe fracture arrest. This result is in agreement with the recent study of Bair et al. (2014) about PST edge effects.

In the future, an in-depth analysis of crack propagation speeds for large slope angles will be carried out in order to distinguish the speed associated to the collapse wave of the slab and the speed associated to its tangential displacement. Finally, different and more complex structures for the WL will also be implemented with the long-term objective to model the structure of the WL directly from segmented micro-tomographic images (Hagenmuller et al., 2013).

Acknowledgements. J. Gaume was supported by the Swiss Government Excellence Scholarship and is grateful to the State Secretariat for Education, Research and Innovation SERI of the Swiss Government. Benjamin Reuter, Eric Knoff and Mark Staples assisted with field data collection.

References

Auld, B. A.: Acoustic Fields and Waves in Solids, Ripol Classic, Russia, 1973. 628

Bair, E. H., Simenhois, R., Birkeland, K., and Dozier, J.: A field study on failure of storm snow slab avalanches, Cold Reg. Sci. Technol., 79, 20–28, 2012. 612

Bair, E. H., Simenhois, R., van Herwijnen, A., and Birkeland, K.: The influence of edge effects on crack propagation in snow stability tests, The Cryosphere, 8, 1407–1418, doi:10.5194/tc-8-1407-2014, 2014. 622, 630, 631

Birkeland, K., van Herwijnen, A., Knoff, E., Staples, M., Bair, E., and Simenhois, R.: The Role of Slab and Weak Layers in Fracture Arrest, edited by: Haegeli, P., 2014 International Snow Science Workshop, Banff, Alberta, 156–163, 2014. 612

Chaudhuri, B., Mehrotra, A., Muzzio, F. J., and Tomassone, M. S.: Cohesive effects in powder mixing in a tumbling blender, Powder Technol., 165, 105–114, 2006. 613

Chiaia, B., Cornetti, P., and Frigo, B.: Triggering of dry snow slab avalanches: stress versus fracture mechanical approach, Cold Reg. Sci. Technol., 53, 170–178, 2008. 611

Crocker, J. C. and Grier, D. G.: Methods of digital video microscopy for colloidal studies, J. Colloid Interf. Sci., 179, 298–310, 1996. 612

Cundall, P. A. and Strack, O. D. L.: A discrete numerical model for granular assemblies, Geotechnique, 29, 47–65, 1979. 613, 614 da Cruz, F., Emam, S., Prochnow, M., Roux, J.-N., and Chevoir, F.: Rheophysics of dense granular materials: discrete simulation of plane shear flows, Phys. Rev. E, 72, 021309, doi:10.1103/PhysRevE.72.021309, 2005. 615

Faug, T., Beguin, R., and Chanut, B.: Mean steady granular force on a wall overflowed by free-surface gravity-driven dense flows, Phys. Rev. E, 80, 021305, doi:10.1103/PhysRevE.80.021305, 2009. 613

Gaume, J., Chambon, G., and Naaim, M.: Quasistatic to inertial transition in granular materials and the role of fluctuations, Phys. Rev. E, 84, 051304, doi:10.1103/PhysRevE.84.051304, 2011. 615

Gaume, J., Chambon, G., Eckert, N., and Naaim, M.: Influence of weak-layer heterogeneity on snow slab avalanche release: application to the evaluation of avalanche release depths, J. Glaciol., 59, 423–437, 2013. 611, 623

Gaume, J., Chambon, G., Eckert, N., Naaim, M., and Schweizer, J.: Influence of weak layer heterogeneity and slab properties on slab tensile failure propensity and avalanche release area, The Cryosphere Discuss., 8, 6033–6057, doi:10.5194/tcd-8-6033-2014, 2014a. 628

Gaume, J., Chambon, G., Reiweger, I., van Herwijnen, A., and Schweizer, J.: On the Failure Criterion of Weak-Snow Layers Using the Discrete Element Method, edited by: Haegeli, P., 2014 International Snow Science Workshop, Banff, Alberta, 2014b. 616

Gaume, J., Schweizer, J., van Herwijnen, A., Chambon, G., Reuter, B., Eckert, N., and Naaim, M.: Evaluation of slope stability with respect to snowpack spatial variability, J. Geophys. Res., 119, 1783–1789, doi:10.1002/2014JF003193, 2014c. 611

Gauthier, D. and Jamieson, B.: Towards a field test for fracture propagation propensity in weak snowpack layers, J. Glaciol., 52, 164–168, 2006. 611, 616

Gauthier, D. and Jamieson, B.: On the sustainability and arrest of weak layer fracture in whumpfs and avalanches, in: Proceedings of the International Snow Science Workshop, Squaw Valley, California, 224–231, 2010. 629

Greene, E., Birkeland, K., Elder, K., Johnson, G., Landry, C., McCammon, I., Moore, M., Sharaf, D., Sterbenz, C., Tremper, and Williams, K: Snow, Weather, and Avalanches: Observational Guidelines for Avalanche Programs in the United States, vol. 150, American Avalanche Association, Pagosa Springs, Colorado, 1–133, 2004. 612

Hagenmuller, P., Chambon, G., Lesaffre, B., Flin, F., and Naaim, M.: Energy-based binary segmentation of snow microtomographic images, J. Glaciol., 59, 859–873, doi:10.3189/2013JoG13J035, 2013. 632

Hagenmuller, P., Theile, T., and Schneebeli, M.: Numerical simulation of microstructural damage and tensile strength of snow, Geophys. Res. Lett., 41, 86–89, doi:10.1002/2013GL058078, 2014. 629

Hamre, D., Simenhois, R., and Birkeland, K.: Fracture speed of triggered avalanches, in: Proceedings ISSW 2014, edited by: Haegeli, P., International Snow Science Workshop, 29 September–3 October 2014, Banff, Alberta, Canada, 174–178, 2014. 630

Heierli, J.: Anticrack Model for Slab Avalanche Release, PhD thesis, Karlsruhe Univ., Karlsruhe, 2008. 628

Heierli, J., Gumbsch, P., and Zaiser, M.: Anticrack nucleation as triggering mechanism for snow slab avalanches, Science, 321, 240–243, doi:10.1126/science.1153948, 2008. 611, 625

Jamieson, B. and Schweizer, J.: Texture and strength changes of buried surface-hoar layers with implications for dry snow-slab avalanche release, J. Glaciol., 46, 151–160, 2000. 641

McClung, D.: Shear fracture precipitated by strain softening as a mechanism of dry slab avalanche release, J. Geophys. Res., 84, 3519–3526, 1979. 611

Podolskiy, E. A., Chambon, G., Naaim, M., and Gaume, J.: A review of finite element modelling in snow mechanics, J. Glaciol., 59, 1189–1201, 2013. 613

Podolskiy, E. A., Barbero, M., Barpi, F., Chambon, G., Borri-Brunetto, M., Pallara, O., Frigo, B., Chiaia, B., and Naaim, M.: Healing of snow surface-to-surface contacts by isothermal sintering, The Cryosphere, 8, 1651–1659, doi:10.5194/tc-8-1651-2014, 2014. 622

Radjai, F. and Dubois, F.: Discrete-Element Modeling of granular Materials, Wiley, ISTE, 2011. 615

Rognon, P., Roux, J.-N., Naaim, M., and Chevoir, F.: Dense flows of cohesive granular materials, J. Fluid Mech., 596, 21–47, doi:10.1017/S0022112007009329, 2008. 613

Roux, J.-N. and Combe, G.: Quasistatic rheology and the origins of strain, CR Phys., 3, 131–140, 2002. 615

Sarkar, A. and Wassgren, C.: Continuous blending of cohesive granular material, Chem. Eng. Sci., 65, 5687–5698, 2010. 613

Scapozza, C.: Entwicklung eines dichte- und temperaturabhängigen Stoffgesetzes zur Beschreibung des visko-elastischen Verhaltens von Schnee, PhD thesis, ETH Zürich, Zürich, Switzerland, 2004. 617

Schweizer, J., Jamieson, B., and Schneebeli, M.: Snow avalanche formation, Rev. Geophys., 41, 1016, doi:10.1029/2002RG000123, 2003. 611

Schweizer, J., Reuter, B., van Herwijnen, A., Jamieson, B., and Gauthier, D.: On how the tensile strength of the slab affects crack propagation propensity, in: Proceedings ISSW 2014, edited by: Haegeli, P., International Snow Science Workshop, 29 September–3 October 2014, Banff, Alberta, Canada, 164–168, 2014. 620

Sigrist, C.: Measurements of Fracture Mechanical Properties of Snow and Application to Dry Snow Slab Avalanche Release, PhD thesis, ETH Zürich, Zürich, 2006. 617

Sigrist, C. and Schweizer, J.: Critical energy release rates of weak snowpack layers determined in field experiments, Geophys. Res. Lett., 34, L03502, doi:10.1029/2006GL028576, 2007. 611

Szabo, D. and Schneebeli, M.: Subsecond sintering of ice, Appl. Phys. Lett., 90, 151916, doi:10.1063/1.2721391, 2007. 622

Timoshenko, S., Goodier, J., and Abramson, H.: Theory of elasticity, J. Appl. Mech., 37, 888, doi:10.1115/1.3408648, 1970. 620, 624

van Herwijnen, A. and Birkeland, K.: Measurements of snow slab displacement in Extended Column Tests and comparison with Propagation Saw Tests, Cold Reg. Sci. Technol., 97, 97–103, 2014. 611, 612

van Herwijnen, A. and Heierli, J.: Measurements of crack-face friction in collapsed weak snow layers, Geophys. Res. Lett., 36, L23502, doi:10.1029/2009GL040389, 2009. 612

van Herwijnen, A. and Jamieson, B.: High speed photography of fractures in weak snowpack layers, Cold Reg. Sci. Technol., 43, 71–82, 2005. 612, 613, 616

van Herwijnen, A. and Jamieson, B.: Snowpack properties associated with fracture initiation and propagation resulting in skier-triggered dry snow slab avalanches, Cold Reg. Sci. Technol., 50, 13–22, 2007. 621

van Herwijnen, A., Schweizer, J., and Heierli, J.: Measurement of the deformation field associated with fracture propagation in weak snowpack layers, J. Geophys. Res., 115, F03042, doi:10.1029/2009JF001515, 2010. 611, 612, 622, 642

Veitinger, J., Sovilla, B., and Purves, R. S.: Influence of snow depth distribution on surface roughness in alpine terrain: a multi-scale approach, The Cryosphere, 8, 547–569, doi:10.5194/tc-8-547-2014, 2014. 630

Zeidler, A. and Jamieson, B.: Refinements of empirical models to forecast the shear strength of persistent weak snow layers: PART B: Layers of surface hoar crystals, Cold Reg. Sci. Technol., 44, 184–193, 2006a. 622

Zeidler, A. and Jamieson, B.: Refinements of empirical models to forecast the shear strength of persistent weak snow layers PART A: Layers of faceted crystals, Cold Reg. Sci. Technol., 44, 194–205, 2006b. 622

Table 1. Mechanical parameters used in the simulations for the contact law. k_n: normal contact stiffness; k_s: tangential contact stiffness; μ: intergranular friction; e: normal restitution coefficient.

k_n ($\mathrm{N\,m^{-1}}$)	k_n/k_s	μ	e
1×10^4	2	0.5	0.1

Table 2. Mechanical parameters used in the simulations for the cohesive law. k_n^b: bond normal stiffness; k_s^b: bond shear stiffness; σ_t: tensile strength; σ_s: shear strength.

	k_n^b (Pa m^{-1})	k_n^b/k_s^b	σ_t (kPa)	σ_t/σ_s
slab	1×10^7–1×10^{10}	2	0–20	2
WL	1×10^{10}	2	1.6	2

Table 3. Table of the parameter values used for Figs. 8 and 9. The symbol "–" means that the associated parameter was varied.

	ρ	E	σ_t	D	D_{wl}	ψ
Fig. 8a	300 kg m^{-3}	–	Inf.	20 cm	4 cm	0°
Fig. 8b	100 kg m^{-3}	4 MPa	Inf.	–/20 cm	4 cm/–	0°
Fig. 8c	–	4 MPa	Inf.	20 cm	4 cm	0°
Fig. 8d	100 kg m^{-3}	4 MPa	Inf.	20 cm	4 cm	–
Fig. 9a	300 kg m^{-3}	–	–	20 cm	4 cm	0°
Fig. 9b	300 kg m^{-3}	4 MPa	–	20 cm	–	0°
Fig. 9c	150 kg m^{-3}	4 MPa	–	20 cm	4 cm	–
Fig. 9d	–	4 MPa	2 kPa	20 cm	4 cm	0°
Fig. 9e	100 kg m^{-3}	4 MPa	1.5 kPa	–	4 cm	0°

Table 4. Average slab thickness as a function of slab density for PST field data.

ρ (kg m^{-3})	100	150	200	250	300
D (cm)	30	40	50	65	80

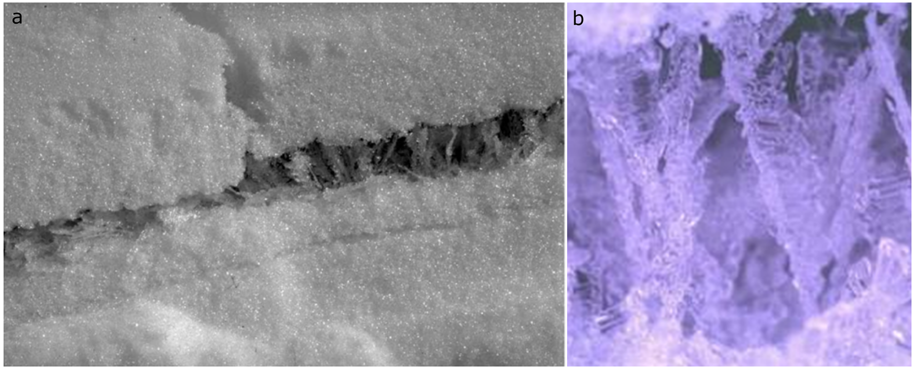

Figure 1. (a) Typical slab – weak layer configuration suitable for avalanche release. The weak layer is composed of surface hoar which is intact on the right and partially ruptured on the left. ©ASARC from Jamieson and Schweizer (2000). **(b)** Zoom on a surface hoar crystal.

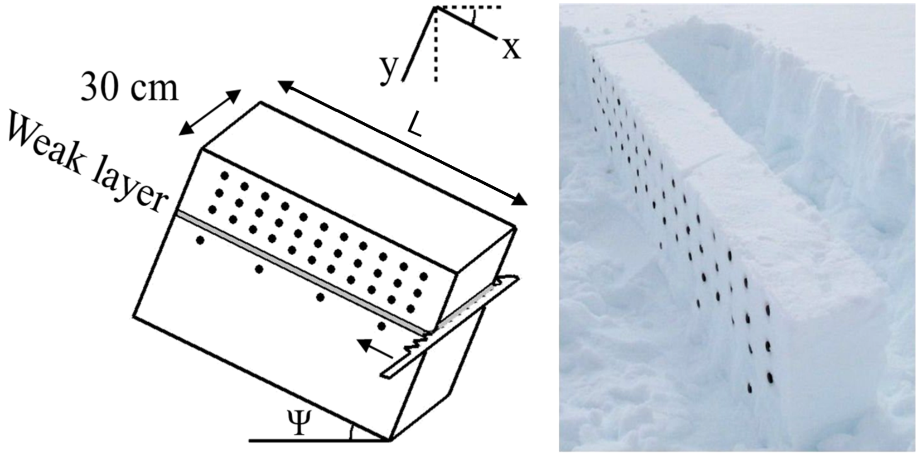

Figure 2. Schematic drawing and picture of the propagation saw test (PST). The black dots are markers used for particle tracking in order to measure the displacement of the slab. The column length is denoted L. Adapted from van Herwijnen et al. (2010).

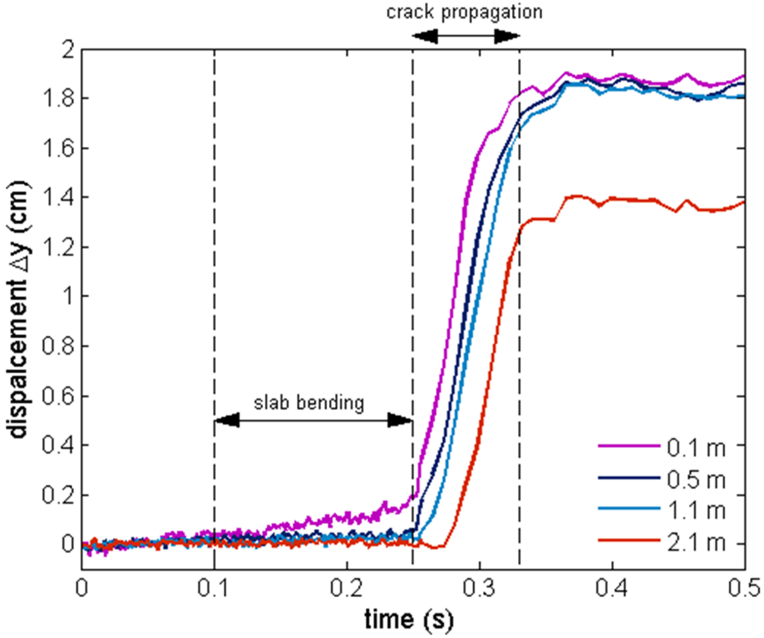

Figure 3. Temporal evolution of the measured vertical displacement Δy for a slab density of $\rho = 240\,\mathrm{kg\,m^{-3}}$. The different curves correspond to different horizontal positions in the slab, from the left-end ($x = 0.1$ m) to the right-end ($x = 2.1$ m).

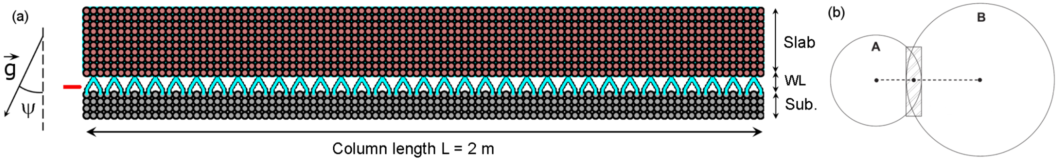

Figure 4. (a) Simulated system of a Propagation Saw Test (PST) composed of a slab, a weak layer and a rigid substratum. The column is 2 m long. **(b)** Illustration of the cohesive contact bond model used in the discrete element simulations.

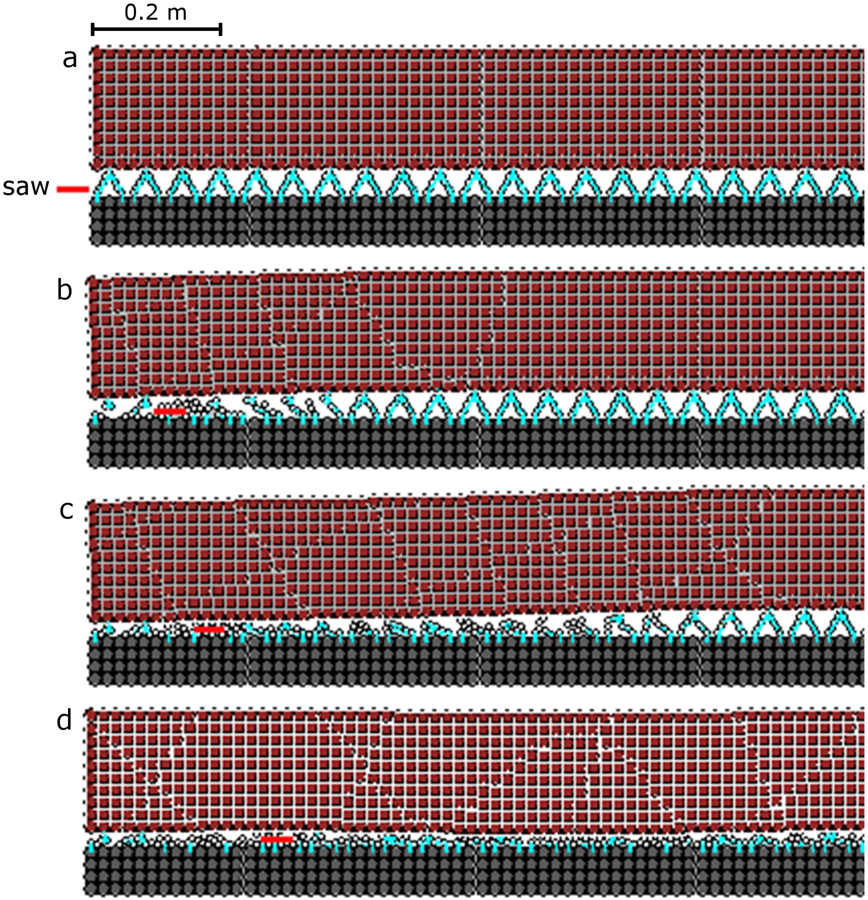

Figure 5. Snapshots of a PST numerical experiment. **(a)** Initial system $t = 0.1$ s, **(b)** onset of crack propagation $t = 0.26$ s, **(c)** dynamic propagation $t = 0.28$ s; **(d)** complete failure of the WL $t = 0.45$ s.

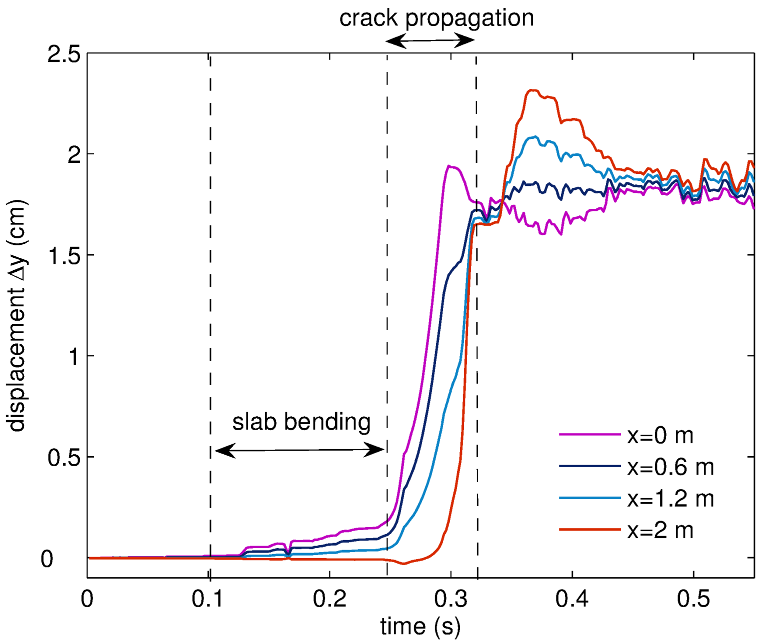

Figure 6. Temporal evolution of the modeled vertical displacement Δy of the slab for a slab density $\rho = 250\,\mathrm{kg\,m^{-3}}$.The different curves correspond to different horizontal positions of the slab, from the left-end ($x = 0\,\mathrm{m}$) to the right-end ($x = 2\,\mathrm{m}$).

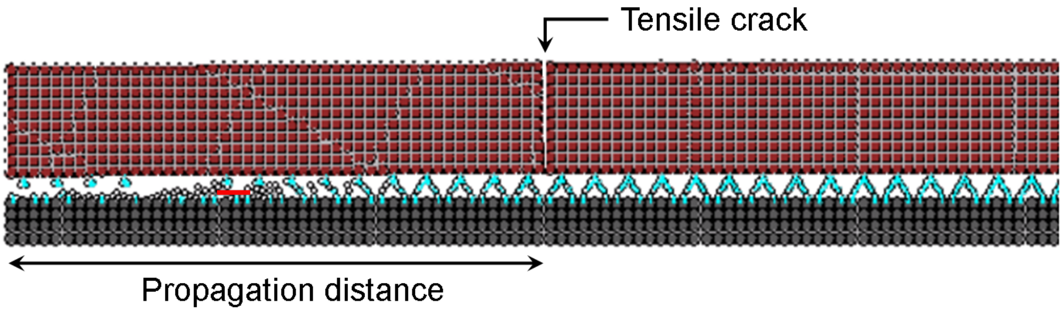

Figure 7. Snapshot of a PST with fracture arrest in the slab due to tensile crack opening.

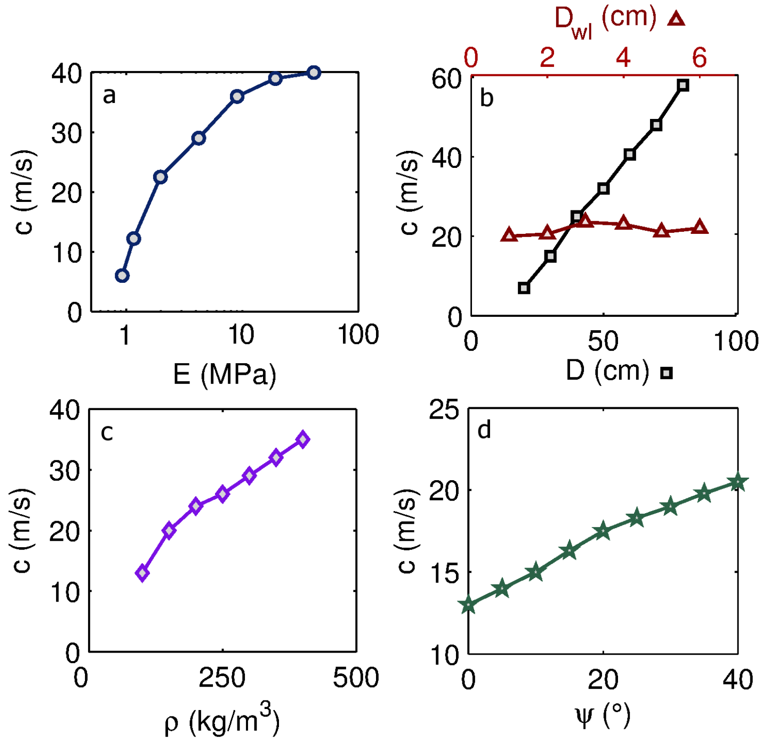

Figure 8. Crack propagation speed c as a function of **(a)** the Young's modulus of the slab E, **(b)** slab and WL thicknesses D and D_{wl}, **(c)** slab density ρ and **(d)** slope angle ψ. The parameters used for these graphics are detailed in Table 3.

TCD
9, 609–653, 2015

Title Page
Abstract | Introduction
Conclusions | References
Tables | Figures
◀| |▶
◀ ▶
Back | Close
Full Screen / Esc
Printer-friendly Version
Interactive Discussion

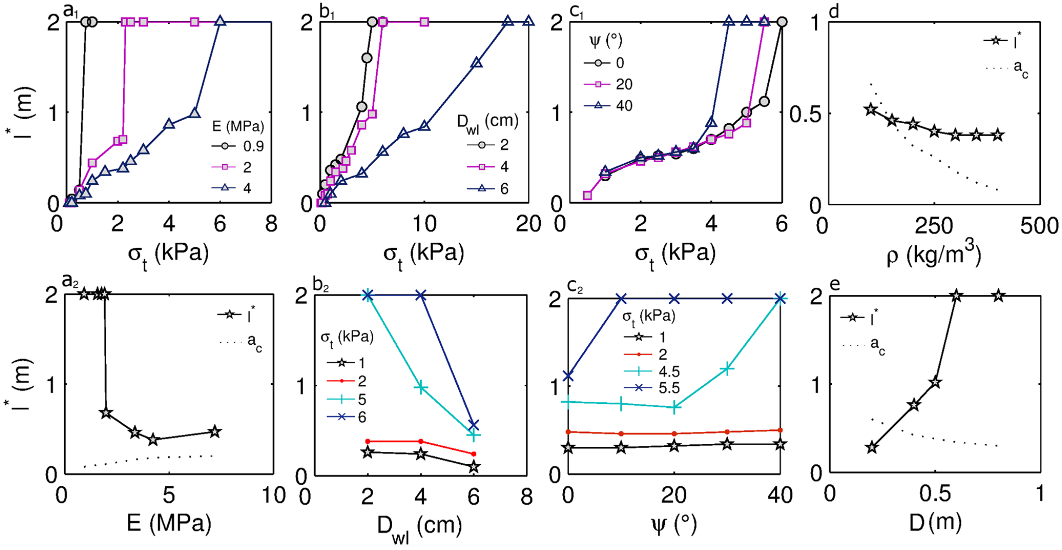

Figure 9. Crack propagation distance l^* as a function of the tensile strength σ_t and the Young's modulus E of the slab **(a_1, a_2)**, the tensile strength σ_t and the WL thickness D_{wl} **(b_1, b_2)**, the tensile strength σ_t and the slope angle ψ **(c_1, c_2)**, slab density ρ **(d)** and slab thickness D **(e)**. The parameters used for these plots are detailed in Table 3.

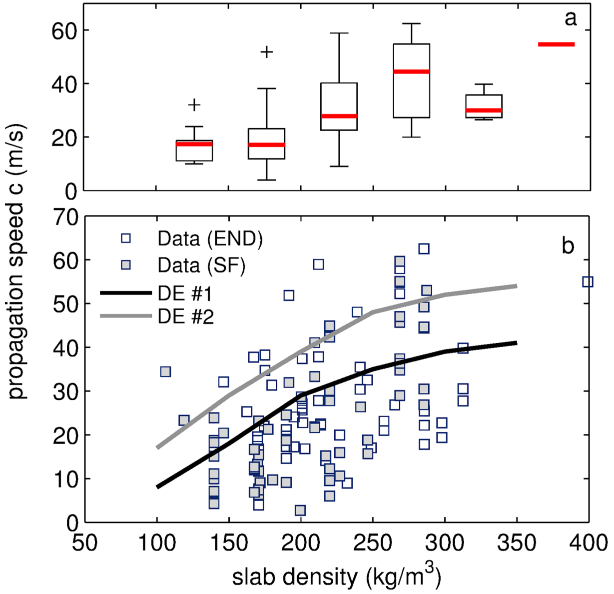

Figure 10. (a) Boxplot of the propagation speed c vs. slab density for all field experiments. The data were grouped by slab density classes of 50 kg m^{-3}. **(b)** Crack propagation speed c vs. slab density ρ. The empty squares correspond to field PST with full propagation (END) and the filled squares correspond to PST with fracture arrest (SF). The black line corresponds to the result of the DE model taking into account the relation between slab density, Young's modulus for a slope angle $\psi = 0^{\circ}$ and a slab thickness $D = 20$ cm (case #1). The gray continuous line corresponds to the result of the DE model taking into account the relation between slab density, Young's modulus and thickness for a slope angle $\psi = 23^{\circ}$ (case #2). The data consist of $N = 121$ PST experiments.

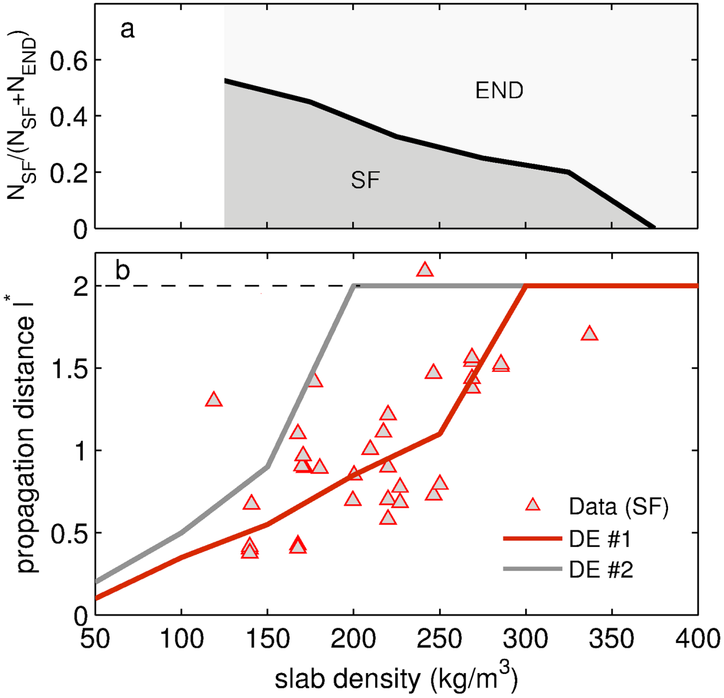

Figure 11. (a) Ratio between the number of experiments with slab fracture N_{SF} and the total number of experiments $N_{SF} + N_{END}$ for different classes of density. **(b)** Propagation distance l^* vs. slab density ρ only for cases with fracture arrest (SF). The red line corresponds to case #1 and the gray line corresponds to case #2. The dashed line correspond to the column length $L = 2$ m in the PST simulations.

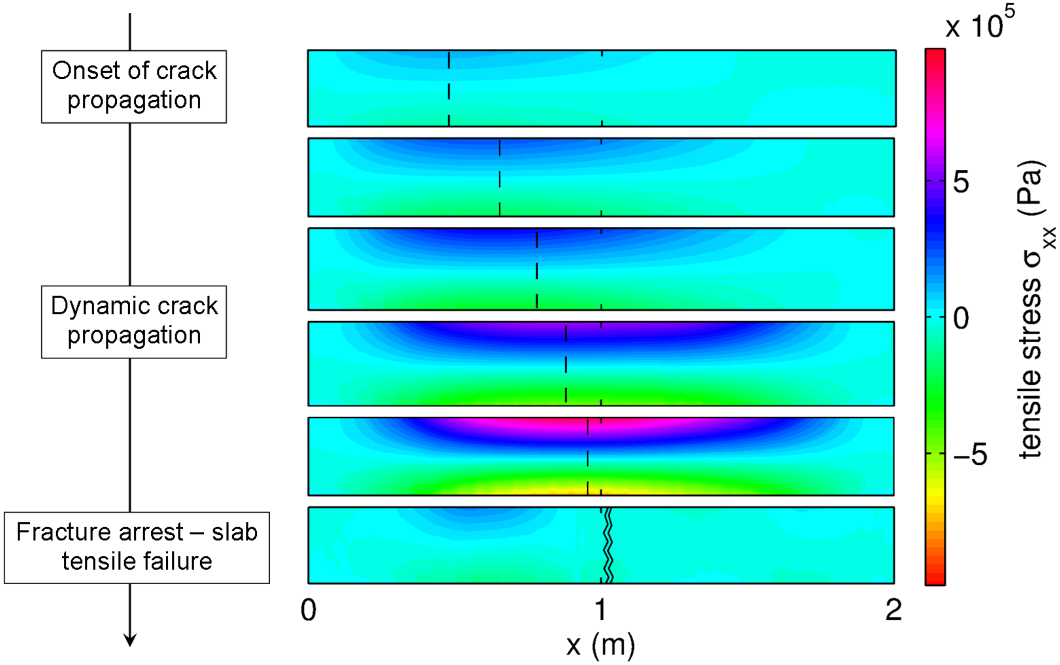

Figure 12. Evolution of the tensile stress σ_{xx} in the slab during the process of crack propagation for a case #1 simulation and a density of 250 kg m^{-3} and a tensile strength of 10 kPa.

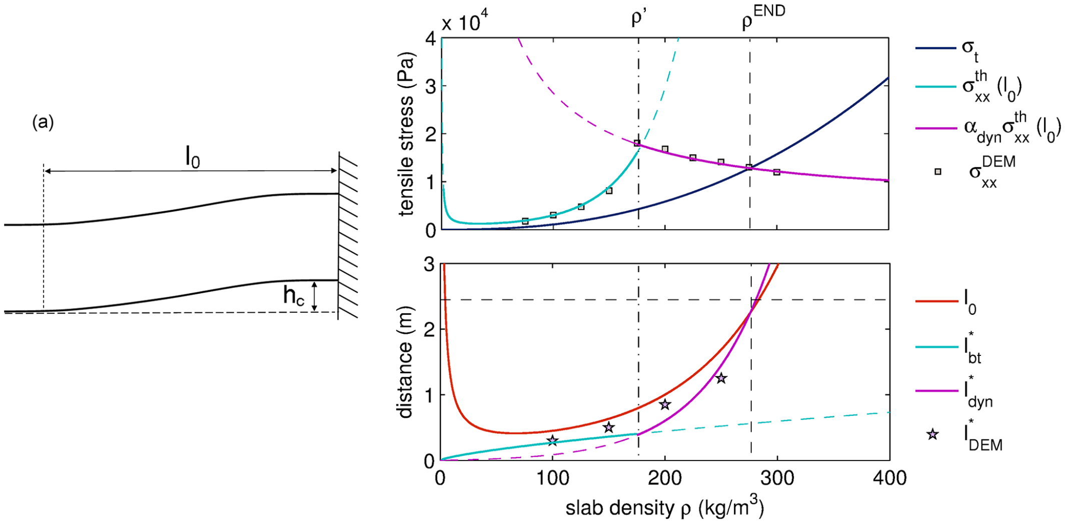

Figure 13. (a) Illustration of the characteristic length l_0 required for the slab to be in contact with the broken WL. h_c represents the collapse height. **(b)** Maximum tensile stress σ_{xx}^{m} as a function of slab density for the discrete element model σ_{xx}^{DEM}, with a purely elastic slab and case #1, according to beam theory $\sigma_{xx}^{th}(l_0)$ and according to Eq. (7) $\alpha_{dyn}\sigma_{xx}^{th}(l_0)$. The tensile strength of the slab σ_t is also represented as a function of slab density ρ. **(c)** Propagation distance for the same cases as in **(b)** plus l_0 as a function of slab density.